RSC Advances

PAPER

View Article Online
View Journal | View Issue

Cite this: *RSC Adv.*, 2025, **15**, 33905

Liquid exfoliated graphene@Ti_3C_2 MXene based dual-signal aptasensing interface for Cd^{2+} and Pb^{2+} simultaneous detection in water and vegetables

Fang Li, [a] Panpan Dong,[b] Zijian Wu, *[bcd] Lu Xue,[b] Mingming Luo[b] and Yijun Tan[b]

Received 6th June 2025
Accepted 11th September 2025

DOI: 10.1039/d5ra04002g

rsc.li/rsc-advances

As ubiquitous pollutants, heavy metal ions can accumulate in the food chain, increasing toxicity through synergistic effects and posing health risks to humans and other organisms. In this study, we successfully developed a dual-signal aptasensing interface for simultaneous detection of cadmium ions (Cd^{2+}) and lead ions (Pb^{2+}). The 2D layered Ti_3C_2 MXene and liquid exfoliated graphene (LEG) composite nanomaterials were employed as ITO electrode modification materials, which exhibited enhanced electrochemical properties. The Cd^{2+}-specific aptamer labeled with Nile blue and Pb^{2+}-specific aptamer labeled with ferrocene bind to their complementary strands immobilized on the electrode surface, resulting in a dual-signal interface. In the presence of target ions, the aptamers specifically recognized and captured the targets, subsequently detaching from the electrode surface, leading to changes in the dual-signals and thereby enabling simultaneous detection of Cd^{2+} and Pb^{2+}. The limits of detection for Cd^{2+} and Pb^{2+} were determined to be 0.689 pM and 1.548 pM, with linear response ranges of 0.1 pM to 10 μM and 0.01 pM to 10 μM. The effectiveness of the proposed aptasensor in determining Cd^{2+} and Pb^{2+} simultaneously in water and vegetables has been demonstrated, providing substantial evidence for its potential application in food safety and environmental monitoring.

1. Introduction

The gradual accumulation of heavy metals in the environment is attributable to human activities, the irrational discharge of wastewater and sludge from industrial production, and the irrational use of pesticides and fertilisers in agricultural production. Heavy metal ions are characterised by their relative stability and non-biodegradability, which results in their prolonged presence in the environment and the potential for toxicity even at low exposure levels.[1] Following entry into the human body, these metals are predominantly transported from the blood to the tissues, thereby contributing to the development of numerous serious diseases. Among the heavy metal ions, cadmium (Cd^{2+}) and lead (Pb^{2+}) ions are of particular concern. According to the World Health Organization (WHO), limits and recommendations for heavy metals in drinking water state that the concentration of Cd^{2+} ions should be less than 3 micrograms per litre (3 ppb), and the concentration of Pb^{2+} ions should be less than 10 micrograms per litre (10 ppb).[2] These ions have been demonstrated to induce developmental abnormalities, neurological and neurobehavioural disorders, immune system disorders, and various types of cancer, with lead in particular causing irreversible neurological damage in children.[3] Furthermore, studies have indicated that the toxicity of multiple metal ions is more pronounced and synergistic than that of a single metal ion.[4] Therefore, it is necessary to develop efficient and sensitive analytical methods for the simultaneous determination of Pb^{2+} and Cd^{2+} in food or water.

In the contemporary era, a plethora of well-established techniques have become prevalent in the field of metal ion analysis, including Cd^{2+}, Pb^{2+}, and others. These include atomic absorption spectrometry,[5] atomic emission spectrometry,[6] X-ray fluorescence spectroscopy,[7] inductively coupled plasma mass spectrometry,[8] surface enhancement Raman scattering,[9] and colorimetric methods.[10] Among these, the atomic absorption spectrometry technique has become a standard analytical method for the determination of heavy metal ions due to its good sensitivity, excellent selectivity, and high accuracy. However, it should be noted that such methods are not without their limitations, frequently requiring large-scale instrumentation, complicated operation procedures, and high levels of expertise, which can be costly and time-consuming and may not always meet the requirements of on-site monitoring. Conversely, the colorimetric method offers several advantages, including ease of operation and intuitive results, which are

[a]*School of Information Engineering, Tianjin University of Commerce, Tianjin, 300134, China*

[b]*Tianjin Key Laboratory of Food Biotechnology, College of Biotechnology and Food Science, Tianjin University of Commerce, 409, Guangrong Road, Tianjin, 300134, China. E-mail: wzjian@tjcu.edu.cn; Tel: +86-18622219597*

[c]*Key Lab of Agricultural Products Low Carbon Cold Chain, Ministry of Agriculture and Rural Affairs, Tianjin, 300134, China*

[d]*Tianjin Key Laboratory of Edible Probiotics, Tianjin, 300134, China*

conducive to immediate on-site detection. However, the majority of contemporary colorimetric methods for the determination of Cd^{2+} and Pb^{2+} do necessitate biologically active substances, which directly results in an increase in the cost of detection and the difficulty of sample preservation.[3]

In recent years, electrochemical sensors have attracted significant attention in the field of heavy metal ion detection, due to their clear advantages over traditional methods. Electrochemical sensors achieve quantitative detection by converting detected signals into electrical signals, including current, potential, resistance, and other electrochemical signals.[11,12] A substantial body of research has demonstrated the merits of this technique, including its simplicity, portability, cost-effectiveness, rapid analysis, low detection limit, sensitivity, and selectivity.[13,14] Nanomaterials are frequently introduced to enhance the sensitivity and selectivity of electrochemical sensors, and obtain a lower limit of detection (LOD). It is important to note that the performance of the sensor in detecting Cd^{2+} and Pb^{2+} is influenced by the type of nanomaterial used. For instance, Nguyen employed gold nanoparticles bearing sodium thiosulfate and surfactant-caps to detect Pb^{2+} with a detection limit of 20 nM.[15] After that, Guo utilized Au@Pd bimetallic nanoparticles for Pb^{2+} detection, achieving a detection limit as low as 0.4 nM.[16] It is noteworthy that the discrepancy in detection limits between these two methods can reach up to 50 times. The range of available nanomaterials is broad, including metal and oxide metal nanoparticles (NPs),[17] carbon-based nanomaterials,[18] conductive polymers,[19] and semiconductors.[20] In recent years, transition metal carbides/carbon-nitrides (MXenes) as a particularly promising class of two-dimensional material, exhibit unique electrical and interfacial properties, such as high conductivity, large specific surface area, and excellent chemical stability.[21–23] The flake surface is rich in functional group sites, which allow for the flexible modulation of surface properties through chemical modifications.[4,24] Meanwhile, carbon-based materials, such as graphene oxide and carbon nanotubes (CNTs), are of significant importance in the field of electrochemical sensors due to their properties and diverse structures. For example, Zukauskas *et al.* developed an electrochemical sensor based on layered $Ti_3C_2T_x$ MXene for the detection of Pb^{2+} in solution, the sensor demonstrated a linear response within the range of 0.15–1.0 μM, exhibiting a sensitivity of 26.7 μA μM^{-1} and a detection limit of 48.7 nM.[25] The sensor's functionality in real-time environmental monitoring underscores the potential of MXene-based sensors for environmental monitoring and public health applications, characterised by their rapid, portable and cost-effective nature. Notably, graphene, with its two-dimensional structure, has garnered significant attention due to its exceptional electrical conductivity, substantial specific surface area, notable mechanical flexibility, self-assembling activity, and remarkable chemical and electrochemical stability.[26–28] Liang *et al.* reported an electrochemical sensor based on reduced graphene oxide (rGO) for the efficient detection of Cd^{2+}.[29] The sensor demonstrated exceptional electron transfer capability, immune to interference, stability, repeatability and reproducibility over the range of 0.92 μg L^{-1} to 36.7 mg L^{-1} with a detection limit of 0.478 μg L^{-1}. Furthermore, it exhibited high recoveries (99.4–102.3%) in real water and rice samples. However, only Ti_3C_2 MXene or graphene exhibits a propensity for stacking, which is a subject of concern. This work proposes an effective strategy to dope LEG into Ti_3C_2 MXene. The utilisation of ultra-thin LEG nanosheets facilitates the interfacial charge transfer in electrochemical reactions, while the introduction of LEG effectively prevents the agglomeration of Ti_3C_2 MXene, thereby ensuring the retention of its favorable electrical conductivity and mechanical properties.

In order to enhance the selectivity capability of these sensors, there has been a recent focus on the integration of organic small molecule probes, proteins, enzymes and DNA probes into the existing electrochemical detection systems.[30] Among these, DNA has attracted much attention due to its chemical stability, ease of mass production and high commercial value. An aptamer is a functional single-stranded DNA or RNA oligonucleotide obtained by *in vitro* screening that is able to form a specific spatial structure by binding to the target through hydrogen bonding, hydrophobic interactions, electrostatic interactions and van der Waals forces. Following binding to the target, the aptamer folds into a unique three-dimensional structure, a process known as 'wrapping' the target molecule.[31] This is accompanied by an increase in the efficiency of electron transfer between the redox marker and the electrode, resulting in the amplification of the assay signal and the sensitive detection of the target. For instance, in the detection of Pb^{2+}, guanine (G)-rich oligonucleotides can be converted to G-quadruplex structures through the induction of Pb^{2+}. This conformational change provides great flexibility in designing electrochemical aptasensors. When the aptamer is labelled and immobilised with a redox group (*e.g.* ferrocene, methylene blue or Nile blue), the conformational change that occurs upon binding the analyte shortens the distance between the redox label and the electrode. This, in turn, induces a change in the current response, which leads to the development of high-performance electrochemical aptasensors.

In this study, the innovative choice of LEG@Ti_3C_2 MXene to modify indium tin oxide (ITO) electrodes is examined.[32] ITO has become one of the most widely used conductors due to its excellent conductivity and high transparency, and its surface can be precisely modified by many cutting-edge technologies.[33–36] The highly specific affinity between the aptamer and the metal ions was exploited for the sensitive detection of Cd^{2+} and Pb^{2+} simultaneously. As illustrated in the scheme diagram, the amino group ($-NH_2$) present on the complementary chain of the metal ion aptamer interacts with the carboxyl group (–COOH) on the surface of the LEG@Ti_3C_2 MXene, thereby facilitating the efficient assembly of the aptamer on the LEG@Ti_3C_2 MXene/ITO electrode. It is noteworthy that the Cd^{2+} and Pb^{2+} aptamers, which are labeled with Nile blue and ferrocene, respectively, can be firmly attached to the LEG@Ti_3C_2 MXene/ITO electrode by virtue of the base complementary pairing. Initially, in the absence of Cd^{2+} and Pb^{2+} ions, the sensor displays a high-intensity electrochemical signal. However, upon the introduction of Cd^{2+} and Pb^{2+}, the metal ions bind specifically to the aptamers, causing

a dissociation of the rigid double-chain structure and a subsequent movement of the aptamers away from the gold electrode. This results in a weakening of the electrochemical signal of the modified electrode. The dynamic changes in peak current before and after recognition can be used for quantitative evaluation of Cd^{2+} and Pb^{2+} simultaneously.

2. Experiment

2.1. Reagents

The oligonucleotides utilized in this study were synthesized and purified by HPLC. (Sangon Biotech Co., Ltd, Shanghai, China). Sequences of the synthesized oligonucleotides are listed in Table S1. Indium tin oxide (ITO) (<6 Ω cm^{-2}, 25 × 10 × 1.1 mm, South China Science and Technology Co. Ltd, China). Ti_3C_2 monolayer Ti_3C_2 MXene (beike 2D materials Co. Ltd, Beijing, China). Graphite powder (Guangdong Hanhui Graphite Co. Ltd, Shenzhen, China). Bovine serum albumin (BSA, Aladdin Chemical Reagent Co., Ltd, Beijing, China). Phosphate buffered solution (PBS, 0.1 M, pH 7.4, Yida Technology Co., Ltd, Quanzhou, China). KCl (North Tianyi Chemical Reagent Factory, Tianjin, China). Potassium ferrocyanide ($K_4[Fe(CN)_6]\cdot 3H_2O$, Kaitong Chemical Reagent Co., Ltd, Tianjin, China). Potassium hexacyanoferrate ($K_3[Fe(CN)_6]$, Bo Hua Chemical Reagent Co., Ltd, Tianjin, China). Acetic acid (HAc, 36%, Guangfu Technology Development Co., Ltd, Tianjin, China). Sodium hydroxide (NaOH, Bohai Chemical Reagent Company Limited, Tianjin, China).

Ferrocene carboxylic acid, 1-thyl-3-[(3-dimethylamino) propyl] carbodiimide (EDC), *N*,*N*′-dicyclohexylacrbodiimide (DCC), *N*-hydroxysuccinimide (NHS), 3-(*N*-morpholino) propane sulfonic acid (MOPs), Nile blue (NB) and $CaCl_2$ were procured from Shanghai Yuanye Bio-Technology Co., Ltd (Shanghai, China). $CdCl_2$, $Co(NO_3)_2$, $CuCl_2$, $MnCl_2$, $PbCl_2$, and $FeCl_2$ were procured from Shanghai Macklin Biochemical Co., Ltd (Shanghai, China).

2.2 Apparatus

A CHI-660E electrochemical workstation (Chenhua Instrument, Shanghai, China) with a three-electrode system (ITO as working electrode, platinum wire as counter electrode, and Ag/AgCl electrode as reference electrode) was utilized for electrochemical measurements in a standard electrochemical cell at room temperature. The morphology and elemental composition of LEG and Ti_3C_2 MXene were observed using scanning electron microscopy (SEM, Hitachi, Ltd) and X-ray photoelectron spectroscopy (XPS, Axis Ultra DLD, Kratos Analytical Ltd, UK). The lettuce was crushed and sheared using a low-temperature ultra-high-pressure cell crusher (JNBIO, China).

2.3. Synthesis of LEG and Ti_3C_2 MXene

The LEG nanomaterials were prepared following the method of Li *et al.*[37] Initially, a graphite solution was prepared by incorporating 0.5 g of graphite powder into 50 mL of a solvent mixture of DMF and deionized water (DIW) (70 vol% DMF, pH 7.3). The graphite flakes were then subjected to sonication for up to 48 h, which induced a high degree of stratification. Following centrifugation at 4000 rpm for 40 min, the LEG solution was successfully obtained in two-thirds of the remaining material.

The synthesis of Ti_3C_2 MXene nanosheets was conducted in accordance with the method previously reported.[38] Initially, 1 g of Ti_3AlC_2 and 1.8 g of lithium fluoride were homogeneously dispersed in 20 mL of hydrochloric acid at a concentration of 9 M. The mixture was then stirred for 26 h at a constant temperature of 35 °C to ensure full reaction of the components. Then, the reaction mixture was washed repeatedly with a sufficient quantity of DIW to effectively remove impurities and collect the solid sample. Thereafter, the collected solid samples were placed in DIW and sonicated for up to 6 h under a nitrogen-protected atmosphere to further exfoliate and disperse the samples to form a more homogeneous dispersion. Following this, the target product, namely Ti_3C_2 MXene nanosheets, was successfully obtained after 24 h of freeze-drying.

The LEG suspension was then mixed with Ti_3C_2 MXene in a 1 : 4 (v/v) ratio and ultrasonicated for a period of 3 h, resulting in the formation of the LEG@Ti_3C_2 MXene composite. The ultrasonic mixing step resulted in a more uniform distribution of LEG on Ti_3C_2 MXene nanosheets and a finer dispersion state, which lays a solid foundation for the optimization of the properties of this nanocomposite.

2.4. *In situ* modification of electroactive tags on aptamers

In order to activate the carboxyl group (–COOH) on Cd-Apt, it was immersed in 100 μL of a 1 μM DCC solution for 2 h. Thereafter, 5 mM NB solution was added and the mixture was immersed for up to 5 h. The NB was labeled at the end of Cd-Apt through a condensation reaction between the $-NH_2$ on NB and the –COOH on Cd-Apt (recorded as Cd-Apt-NB).

A mixture of 100 μL containing 20 mM EDC and 10 mM NHS was prepared and added to the Pb-Apt solution. Subsequently, 15 mg of Fc-COOH was added to the above solution, sonicated for 1 h, and then shaken for 8 h. The Fc was labeled at the end of Pb-Apt through a condensation reaction between the –COOH on Fc and the $-NH_2$ on Pb-Apt (recorded as Pb-Apt-Fc).

2.5. Fabrication of the duplexed-electrochemical aptasensor

The cleaning of ITO glass electrodes was conducted in the following manner: the ITO electrodes were subjected to ultrasonic cleaning with acetone, anhydrous ethanol, and deionized water, with the ultrasonic cleaning being performed for a duration of 15 min. Subsequent to the cleaning process, the ITO electrodes were dried in an oven for future use.

As outlined in Scheme 1, the fabrication process of the duplexed-electrochemical aptasensor commenced with the modification of the ITO surface with 80 μL of LEG@Ti_3C_2 MXene nanocomposites (LEG@Ti_3C_2 MXene/ITO), followed by rinsing and drying at room temperature. Subsequently, 20 μL of 2 μM cDNA solution (a mixture of Cd-cDNA and Pb-cDNA) was drop-coated onto the electrode (cDNA/LEG@Ti_3C_2 MXene/ITO). Then, BSA (10 μL, 1 mM) was dropped onto the surface of the electrode and incubated for 1 h (BSA/cDNA/LEG@Ti_3C_2 MXene/

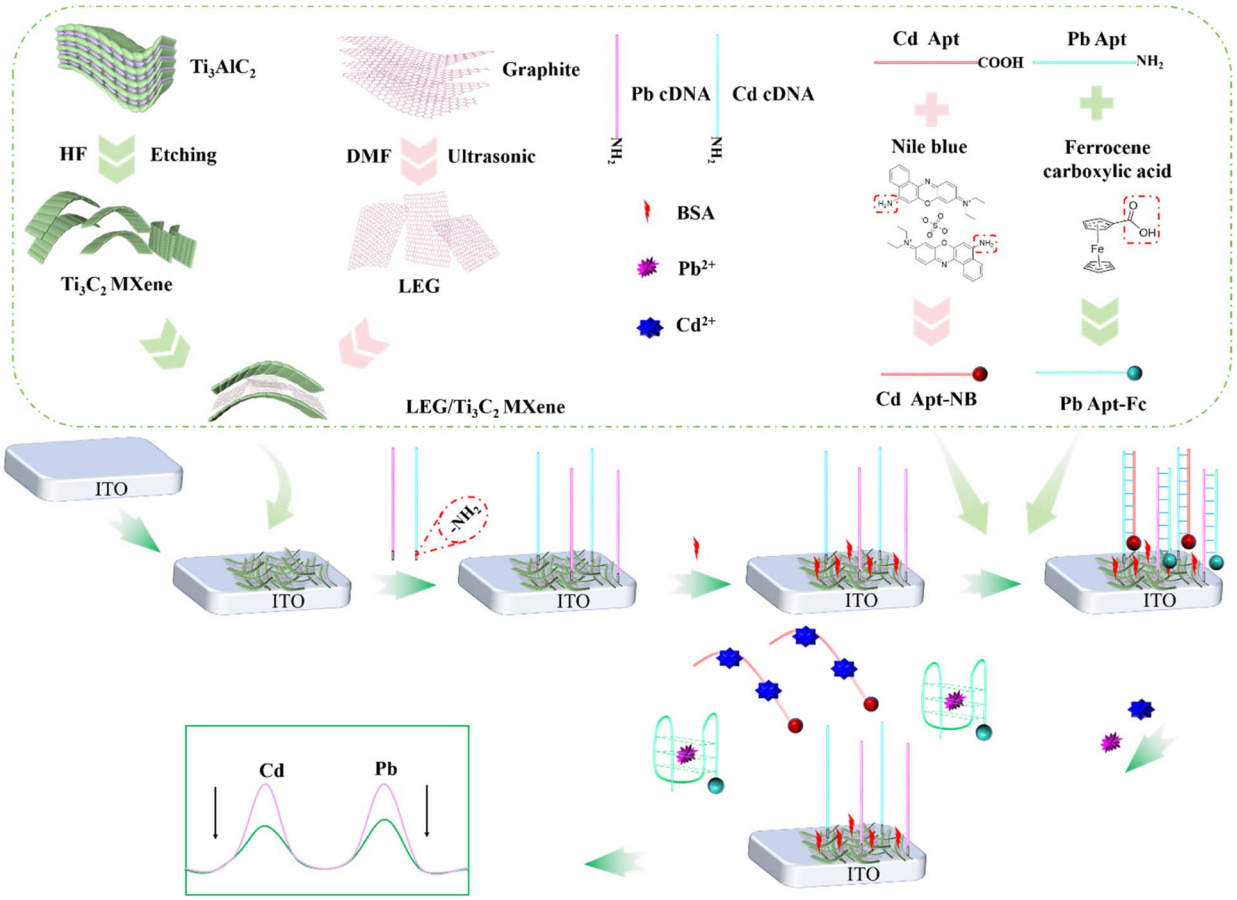

Scheme 1 Schematic diagram of the duplex electrochemical aptasensor for simultaneous detection of Cd^{2+} and Pb^{2+} ions.

ITO) to prevent nonspecific adsorption. Subsequently, 20 μL of 1 μM aptamer solution (a mixture of Cd-Apt-NB and Pb-Apt-Fc) was drop-costed on the electrode (Apt/BSA/cDNA/LEG@Ti_3C_2 MXene/ITO), and the electrode was then meticulously cleaned with MOPs. This process resulted in sensing interfaces with two types of electroactive aptamers. The electrode was rinsed with PBS buffer following each modification step and characterized using cyclic voltammetry (CV) and electrochemical impedance spectroscopy (EIS).

2.6. Electrochemical measurement

The prepared Apt/BSA/cDNA/LEG@Ti_3C_2 MXene/ITO electrode was immersed in the mixture of Cd^{2+} and Pb^{2+} solutions for a period of 30 min, after which it was washed with a solution of PBS. CV measurements were then taken in 1 mM $K_3Fe(CN)_6$/$K_4Fe(CN)_6$/0.1 M KCl, over a potential range of −0.6 to +0.8 V, at a scan rate of 100 mV s^{-1}. Electrochemical DPV measurements were conducted at voltages ranging from −0.6 to +0.6 V, with a pulse width of 0.2 s. Each sample was examined on three occasions for detection, and the value obtained was the average of the three results. It is important to note that all measurements were performed at room temperature.

2.7. Real sample pretreatment

To verify the practicality of the duplexed-electrochemical aptasensor, a series of real samples (tap water, river water, and lettuce) were tested. Laboratory tap water, river water from the Twin Lakes at Tianjin University of Commerce, and lettuce purchased from a local market were used. Prior to analysis, the water samples were centrifuged at 10 000 rpm for 5 min and then filtered through a 0.22 μm membrane to remove any suspended matter.[39] For the processing of lettuce samples, 10 g of lettuce was accurately weighed and added to 100 mL of PBS.[31] Afterwards, the lettuce was crushed, filtered, and further processed using a cell disruptor. Finally, the sample was filtered through a 0.22 μm membrane to remove particulate matter.

3. Results and discussion

3.1. Characterizations of LEG and Ti_3C_2 MXene

The surface morphology of LEG, Ti_3C_2 MXene, and LEG@Ti_3C_2 MXene was observed by means of SEM. As demonstrated in Fig. 1A, numerous graphene flakes in the form of small fragments are clearly visible, thus confirming the successful implementation of the LEG preparation process. In addition, the structure of the self-supported Ti_3C_2 MXene flakes is clearly visible, and the curled edges of the flakes significantly highlight

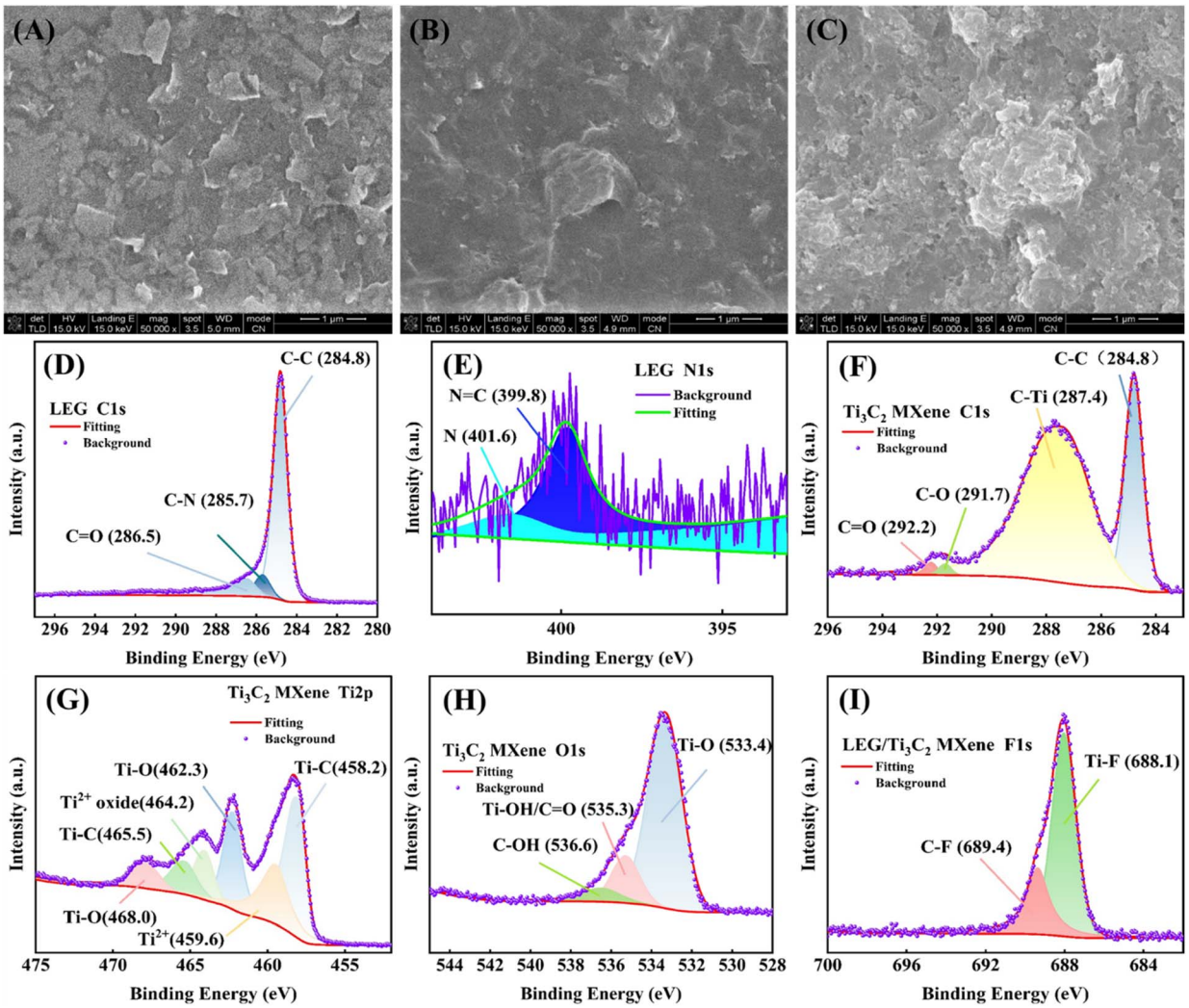

Fig. 1 SEM images of (A) LEG, (B) Ti_3C_2 MXene, (C) LEG@Ti_3C_2 MXene. (D) C 1s spectra of LEG; (E) N 1s spectra of LEG; (F) C 1s spectra of LEG@Ti_3C_2 MXene; (G) Ti 2p spectra of Ti_3C_2 MXene; (H) O 1s spectra of Ti_3C_2 MXene; (I) F 1s spectra of LEG@Ti_3C_2 MXene Ti_3C_2 MXene.

the flexible nature of the film (Fig. 1B). Collectively, these observations indicate the successful preparation of monolayer Ti_3C_2 MXene. When LEG and Ti_3C_2 MXene are mixed, the material exhibits a rough, three-dimensional layer morphology (Fig. 1C). This clearly indicates that LEG plats a key role as an expander in this process, successfully penetrating the lamellar structure of Ti_3C_2 MXene, thereby increasing the layer spacing and ultimately contributing to the formation of the encapsulation structure of Ti_3C_2 MXene on LEG. This increased interlayer spacing is advantageous for the diffusing and transport of electrolyte ions and significantly improves the accessibility of Ti_3C_2 MXene nanosheets to electrolyte ions.[40] Consequently, the material can be applied directly to the electrode fabrication process without the need for additional processing steps.

In order to verify the presence of a single-layer structure in Ti_3C_2 MXene, XRD testing was conducted (Fig. S1). Following the etching of the Al layer of Ti_3AlC_2, it was observed that the characteristic peak of Ti_3C_2 MXene (002) shifted from 9.4° to a lower value of 7.1°. In addition, the characteristic peak (104) has almost disappeared, indicating a structural transformation of the material. This phenomenon is attributed to the replacement of Al elements in Ti_3C_2 MXene and the introduction of –OH, –O, and –F groups, thereby confirming the successful synthesis of Ti_3C_2 MXene.[41]

Fig. S2 showed the FT-IR spectra of the composite material LEG@Ti_3C_2 MXene, cDNA/LEG@Ti_3C_2 MXene, and aptamer-immobilised cDNA/LEG@Ti_3C_2 MXene. It can be observed that after modifying cDNA on the surface of LEG@Ti_3C_2 MXene, the extensive –OH groups on the material surface participate in hydrogen bonding or covalent coupling with cDNA, causing a slight shift in the broad peak at 3400 cm^{-1}, indicating that cDNA has been successfully functionalised on LEG@Ti_3C_2 MXene. Subsequently, NB and Fc-modified aptamers (Cd-Apt-NB and Pb-Apt-Fc) were immobilised on cDNA/LEG@Ti_3C_2 MXene, and peaks at 1045 cm^{-1}, 1108 cm^{-1}, and 1648 cm^{-1}, which are attributed to the stretching vibrations of the carboxyl C=O group on NB, while the peak at 3450 cm^{-1} corresponds to the free hydroxyl –OH group. Fc exhibited characteristic peaks

below 1500 cm^{-1}, with the 1108 cm^{-1} peak corresponding to the CH_2X bond and the 875 cm^{-1} peak representing the "out-of-plane" structure of the C–H bond. These results indicated that cDNA and the aptamer successfully labelled LEG@Ti_3C_2 MXene.[42,43]

To thoroughly analyze the surface chemical bonding properties of LEG, Ti_3C_2 MXene, and LEG@Ti_3C_2 MXene composites, XPS analysis was further conducted in this study. The bonding properties of the different compositions were elaborated based on the chemical shifts of the elements by fitting the electronic binding energy curves of C 1s, N 1s, Ti 2p, O 1s, and F 1s (Fig. 1D–I). First, the elemental composition of LEG was analyzed by its core spectra (Fig. 1D). In the C 1s core spectra, the fitted peaks at 284.8 and 285.7 eV correspond to the carbon elements of LEG in the sp^2 and sp^3 states, respectively, while the fitted peak of C 1s at 286.5 eV indicates the presence of small amounts of oxygen atoms during the liquid stripping step as well as the DMF pretreatment of the substrate. The N 1s spectra (Fig. 1E) show a N 1s fitted peak at 399.8 eV attributed to the N═C triggered by the DMF reaction, while the peak at 401.6 eV corresponds to the graphitic nitrogen, presumed to be caused by the N-atom doping during the ultrasonic stripping process.

The results of the XPS analysis of the Ti_3C_2 MXene layer are displayed in Fig. 1F. The high-resolution XPS spectra in the C 1s region of the Ti_3C_2 MXene powder exhibited four prominent peaks at 284.8, 287.6, 291.7 and 292.2 eV, originating from Ti–C, C–C, C–O, and C═O/COO– respectively. The presence of C–O can be attributed to TiO_2 and carbon atom networks, which may be produced by the oxidation reaction of Ti_3C_2 MXene.[44] As demonstrated in Fig. 1G, the high-resolution spectra of Ti 2p of Ti_3C_2 MXene display two peaks at 458.2 eV and 465.5 eV, originating from the Ti–C bond within the host structure. Conversely, the peaks at 459.6, 462.3, 464.2, and 468.0 eV are attributed to the Ti–O bonds present on the surface of Ti_3C_2 MXene. The high-resolution spectra of the O 1s region in Fig. 1H demonstrate the presence of Ti–O, Ti–OH, C–O, and C–OH bonds. Fig. 1I clearly shows Ti–F, confirming the presence of F groups due to the etchant. Furthermore, when LEG was mixed with Ti_3C_2 MXene, a new C–F bond peak was identified at 689.4 eV in the high-resolution spectrum of F 1s. In combination with the aforementioned XPS analysis results, this study provides unequivocal evidence that the synthesis of LEG@Ti_3C_2 MXene composites has been successfully accomplished.

3.2. Electrochemical characterization of the duplexed-electrochemical aptasensor

The stepwise fabrication process of the aptasensor was characterized by means of CV and EIS, as illustrated in Fig. 2A. Each curve exhibits a pair of distinct redox peaks, corresponding to the electrochemical redox process of the $[Fe(CN)_6]^{3-/4-}$ couple. When modifying LEG@Ti_3C_2 MXene (curve b) on the surface of bare ITO (curve a), the peak current increased due to its excellent conductivity, which may be attributed to the synergetic effect of different components. In addition, as can be seen from Fig. S3, the conductive effect of the composite LEG@Ti_3C_2 MXene was higher than that of LEG and Ti_3C_2 MXene. In the instance of modifying the LEG@Ti_3C_2 MXene/ITO surface with Cd-cDNA and Pb-cDNA (curve c), a substantial reduction in the redox peaks was observed when the $–NH_2$ was covalently immobilized on the nanomaterials, which contained a substantial number of –COOH. This is attributable to the fact that the grafted negatively charged nucleic acid aptamer blocked the transfer of electrons to the surface of the electrodes. This finding serves as evidence that the cDNA had been successfully anchored on the surface of the modified electrode. Subsequent modification of the electrode by BSA resulted in a further reduction in the electrochemical response (curve d). This decline can be explained by the occupation of unoccupied sites on the electrode surface by the non-conductive BSA, signifying that the BSA has also effectively modified the electrode surface. The subsequent addition of Cd-Apt-NB and Pb-Apt-Fc were added to form double-stranded DNA (dsDNA) resulted in an electron transfer impediment, leading to a further decrease in peak current (curve e). Finally, when a mixture of Cd^{2+} and Pb^{2+} was dripped onto the electrode surface, the dsDNA dissociated and the peak current rose back up to a level close to that when only cDNA and BSA were modified (curve f). This finding indicates that the Cd^{2+} and Pb^{2+} do indeed bind to their aptamers, effectively preventing them from approaching the electrode surface.

EIS is a sophisticated analytical instrument that provides precise information regarding alterations occurring at the electrode interface. In the high-frequency region of the EIS spectrum, the change in semicircle diameter can directly reflect the increase or decrease in interfacial charge transfer resistance (R_{ct}). As demonstrated in Fig. 2B, the bare ITO electrode (curve a) exhibited a smaller semicircular structure with an R_{ct} value of approximately 36 Ω. However, when the ITO electrode was modified by LEG@Ti_3C_2 MXene nanocomposites, its semicircle diameter (curve b) decreased significantly and the R_{ct} value reduced to 9 Ω, a phenomenon attributed to the excellent electrical conductivity of LEG@Ti_3C_2 MXene nanocomposites. Following the immobilization of the Cd-cDNA and Pb-cDNA on the surface of LEG@Ti_3C_2 MXene/ITO electrodes, an increase in the value of R_{ct} to 18 Ω (curve c) was observed, which can be attributed to the negatively charged phosphate backbone that exerted a hindering effect on the electron transfer process of the $[Fe(CN)_6]^{3-/4-}$ redox probe. Following the addition of BSA and subsequent incubation, an increase in the R_{ct} value to 180 Ω was observed (curve d), indicating that BSA successfully modified the electrode surface and hindered electron transfer. The subsequent addition of Cd-Apt-NB and Pb-Apt-Fc (curve e) resulted in hybridization to form double chains on the electrode surface, leading to an increase in the R_{ct} value to 412 Ω. This change may be related to the repulsion between the redox probe and the negatively charged DNA phosphate backbone, as well as the blocking effect on the electrode surface. However, following the incubation of Cd^{2+} and Pb^{2+} on the modified electrode surface (curve f), a decrease in R_{ct} value to 297 Ω was observed. This phenomenon can be attributed to the combination of Cd^{2+} and Pb^{2+} with aptamers immobilized on the electrode surface, forming Cd^{2+}/Cd-Apt-NB and Pb^{2+}/Pb-Apt-Fc complexes. The formation sites of these complexes exist at a distance from the

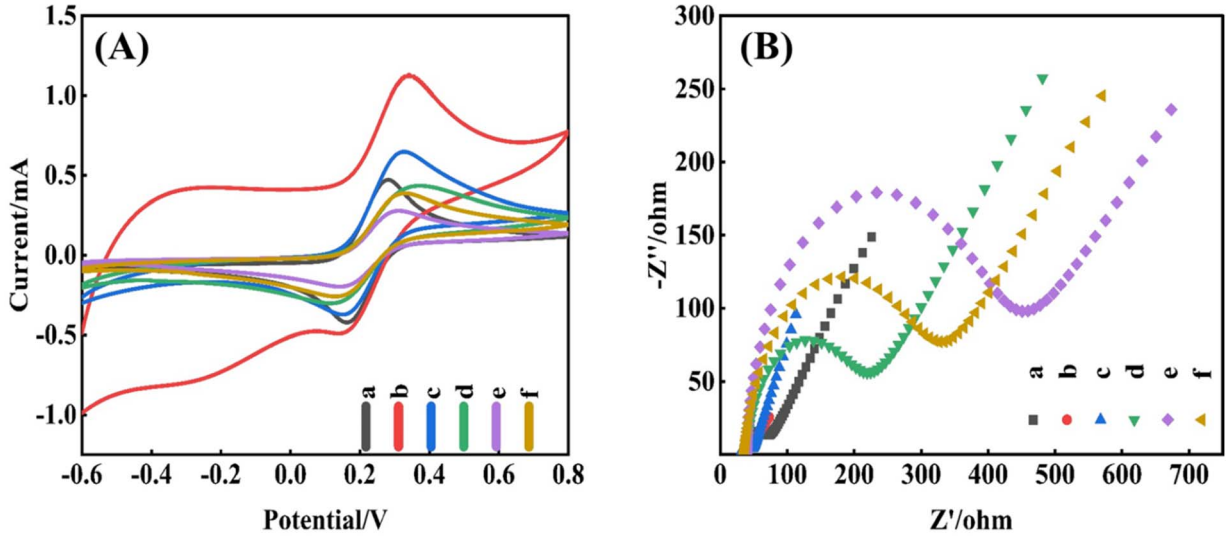

Fig. 2 CV (A) and EIS (B) curves of different modified electrodes in 1 mM $K_3Fe(CN)_6/K_4Fe(CN)_6$/0.1 M KCl. (a) Bare ITO, (b) LEG@Ti_3C_2 MXene/ITO, (c) cDNA/LEG@Ti_3C_2 MXene/ITO, (d) BSA/cDNA/LEG@Ti_3C_2 MXene/ITO, (e) Apt/BSA/cDNA/LEG@Ti_3C_2 MXene/ITO, (f) Pb^{2+} and Cd^{2+}/Apt/BSA/cDNA/LEG@Ti_3C_2 MXene/ITO.

electrode surface, thereby reducing the resistance. The EIS results obtained are in excellent agreement with the CV measurements, strongly demonstrating the successful development of the constructed electrochemical aptasensor.

3.3. Optimization of the experimental conditions

To achieve optimal analytical performance, a series of experiments were conducted to investigate the influence of several parameters: the concentration and incubation time of Cd-cDNA and Pb-cDNA, the concentration and immobilization time of Cd-Apt and Pb-Apt, the binding time of the metal ions to the aptamers and the effect of different pH conditions.

The immobilization condition of cDNA is pivotal to optimal sensor performance. Initially, the concentration of the cDNA solution employed for immobilization was investigated, as elevated concentrations result in wastage, while low concentrations result in an excess of unspecific sites on the LEG@Ti_3C_2 MXene platform. This may result in a substantial background when utilizing the electrodes for the detection of the target analyte. The LEG@MXene/ITO electrodes were incubated for an equivalent duration with varying concentrations of the cDNA solution. The CV was employed to monitor the signal of each electrode. As illustrated in Fig. 3A, the peak current exhibited a pronounced increase with increasing cDNA concentration from 0.5 to 2 μM, and the modified electrode exhibited the most substantial electrochemical signal at 2 μM cDNA. This phenomenon can be attributed to the negative charge of the cDNA, which hinders the access of $[Fe(CN)_6]^{4-/3-}$ to the electrode surface. Conversely, when the cDNA concentration was increased from 4 to 8 μM, the peak current decreased. Consequently, 2 μM was determined as the optimal concentration for cDNA immobilization. The incubation time for cDNA immobilization was also investigated, with the LEG@MXene/ITO electrodes being incubated in 2 μM of cDNA solution at different time, followed by CV detection. With the increase of incubation time, the chemical signals of the modified electrodes were rapidly enhanced and reached the maximum value within 90 min, as shown in Fig. 3B, which indicated the time required for the complete binding reaction of LEG@MXene with the inter-cDNA. Consequently, the cDNA fixation time was set at 90 min.

To ascertain the optimum concentration of aptamer that can fully react with cDNA, an increasing dose of aptamer was gradually added to the electrode surface. As demonstrated in Fig. 3C, the modified electrode exhibited the maximum electrochemical signal at a concentration of 1 μM aptamer. At a low concentration of the aptamer, it could not be fully bound to the cDNA, and the electrochemical signals were decreased significantly once the concentration of the aptamer exceeded 1 μM. This phenomenon can be attributed to the interaction between the positively charged aptamer and the negatively charged phosphate group of the cDNA, which results in an increase in background current noise and a decrease in electrochemical signals. This observation indicates that the binding affinity of aptamer and cDNA at this concentration is at its optimal level. Furthermore, the binding time between aptamer and cDNA was thoroughly investigated as illustrated in Fig. 3D. It was established that an optimal concentration of 1 μM was required for the immobilization of aptamer and that the BSA/cDNA/LEG@MXene/ITO electrodes were incubated in 1 μM aptamer solution for different durations. The experimental results demonstrated that the chemical signals of the modified electrodes climbed to the maximum value within 60 min.

The electrochemical signals of the electrodes were monitored at various intervals following the introduction of Cd^{2+} and Pb^{2+}. It was found that the current of the modified electrodes showed a rapid increase with the incubation process and reached a peak at 20 min (Fig. 3E). Subsequent analysis

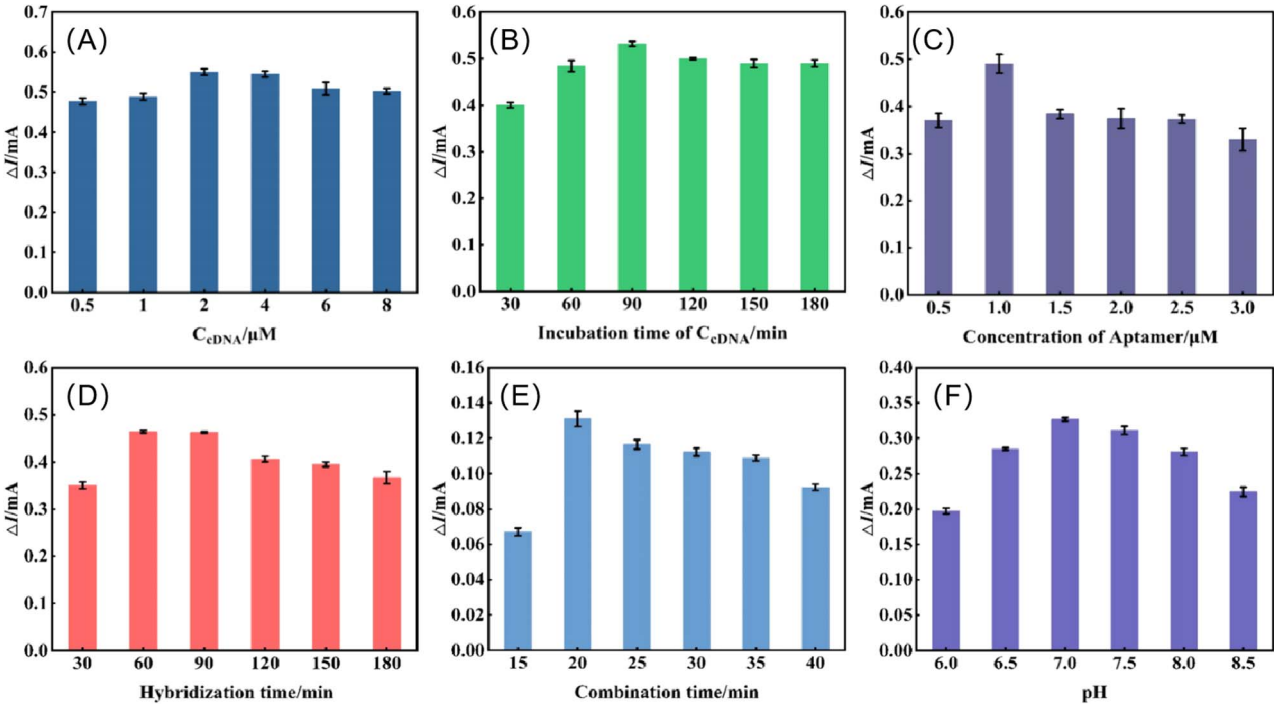

Fig. 3 Factors involved in the electrochemical signal of the electrode. (A) cDNA concentration; (B) cDNA incubation time; (C) aptamer concentration; (D) cDNA and aptamer hybridization time; (E) aptamer–ion combination time; (F) reaction buffer pH.

identified this 20 min period as the optimal time for effective binding of ions to the aptamer. In addition, the ensemble sensor was examined in a variety of solutions, with pH values ranging from 6.0 to 8.5, in order to ascertain the effect of differing pH values on the aptasensors. As demonstrated in Fig. 3F, the current signals exhibited a substantial enhancement when the pH value was incrementally increased from 6.0 to 7.0; however, a notable decline was observed thereafter. This experimental phenomenon is consistent with the fact that DNA strands are deconvoluted, less stable, and more susceptible to breakage at high pH. Conversely, under acidic conditions, the presence of hydrogen ions leads to the destabilisation of hydrogen bonds, resulting in deconjugation, deformation, and even degradation of the DNA molecular structure.[45] The selection of pH 7.0 as the subsequent experiments' location was informed by these considerations.

3.4. Sensitivity of the developed duplexed-electrochemical aptasensor

The DPV technique is an electrochemical method that has been demonstrated to offer several advantages, including low capacitance, low background response, and high current sensitivity. Under optimized experimental conditions, the DPV technique was utilized to characterize the performance of a developed duplexed-electrochemical aptasensor at varying concentrations of Cd^{2+} and Pb^{2+}. As illustrated in Fig. 4A, a series of DPV curves corresponding to the different concentrations of Cd^{2+} and Pb^{2+} were presented. The duplexed-electrochemical aptasensor displayed two distinct oxidation peaks at −0.35 V and +0.3 V, respectively. The significant peak-to-peak separation (ΔE_p = 65 mV) suggested the absence of signal interference between the two labels, emphasizing the sensor's precision and reliability. The peak current exhibited a negative correlation with the concentration of Cd^{2+} and Pb^{2+}, within the range of 0.001 pM to 10 μM, suggesting that Cd-Apt-NB binds to Cd^{2+}, forming a folded structure that results in the NB being directed away from the electrode surface. Concurrently, the reaction of the flexible Pb-Apt-Fc with Pb^{2+} leads to its transformation into a G-quadruplex structure, causing the Fc to also move away from the electrode surface. Further analysis revealed that the peak current I_{NB} and I_{Fc} showed a good linear relationship with the logarithmic value of Cd^{2+} concentration (0.1 pM to 10 μM) ($\lg C_{Cd^{2+}}$) and with the logarithmic value of Pb^{2+} concentration (0.01 pM to 10 μM) ($\lg C_{Pb^{2+}}$) (Fig. 4B and C). The regression equations were found to be $Y = -0.011X + 0.139$ ($R^2 = 0.998$) and $Y = -0.013X + 0.160$ ($R^2 = 0.996$), respectively. The LOD were measured to be as low as 0.689 pM for Cd^{2+} and 1.548 pM for Pb^{2+}, with a signal-to-noise (S/N) ratio of 3.

Tables S2 and S3 presented a comparison of several electrochemical aptasensors for the detection of Cd^{2+} and Pb^{2+}, encompassing pivotal parameters such as linear range, detection limit, and detection technique. Furthermore, Table S4 discussed the relevant performance parameters of other dual-signal aptasensors. A comparison of the aptasensors prepared in this paper with those reported in other references reveals that the sensors prepared in this paper demonstrate a wide linear range and lower detection limit. This finding suggested that the sensitivity of these sensors has been significantly enhanced. In comparison with the WHO and the national standard of the

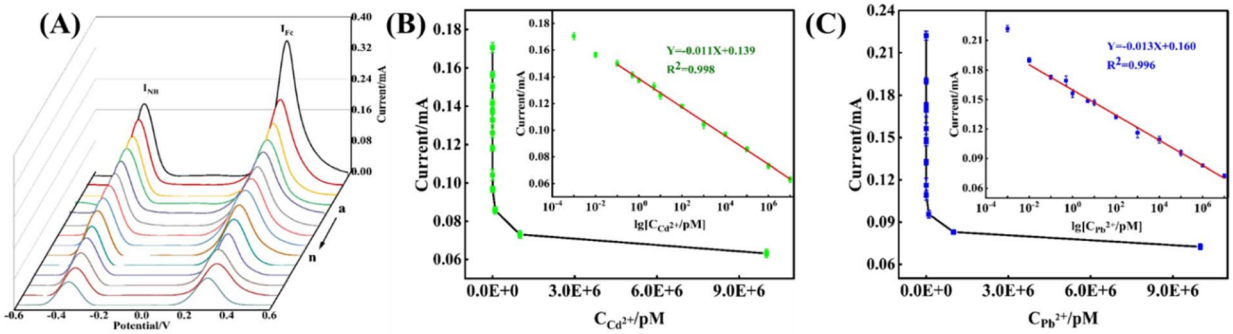

Fig. 4 (A) Dependence of DPVs of the aptasensor on Pb^{2+} and Cd^{2+}: 0.001 pM, 0.01 pM, 0.1 pM, 0.5 pM, 1 pM, 5 pM, 10 pM, 100 pM, 1 nM, 10 nM, 100 nM, 1 μM, 10 μM in 0.1 μM, Tris–HCl buffer. (B) and (C) The calibration curve of DPV peak current as a function of Cd^{2+} and Pb^{2+} concentration. The inset shows the linear relationship part between the I_{MB} *versus* lg $C_{Cd}{}^{2+}$ and the linear relationship part between the I_{Fc} *versus* lg $C_{Pb}{}^{2+}$.

Ministry of Health of China, the detection levels of Cd^{2+} and Pb^{2+} were lower than the detection limits of both in drinking water, which highlights the advantages of the dual-signal sensor for simultaneous analysis of Cd^{2+} and Pb^{2+}. The dual electrochemical aptasensor has been demonstrated to exhibit excellent performance for the following reasons: firstly, the LEG@Ti_3C_2 MXene nanocomposite possesses a substantial surface area, which can provide ample active sites and can be utilized as a substrate to enhance the loading capacity of aptamer, thereby effectively enhancing the sensitivity of the aptasensor. Secondly, the unique spatial structure of the aptamer and the strong affinity between the aptamer and the metal ions (Cd^{2+} and Pb^{2+})

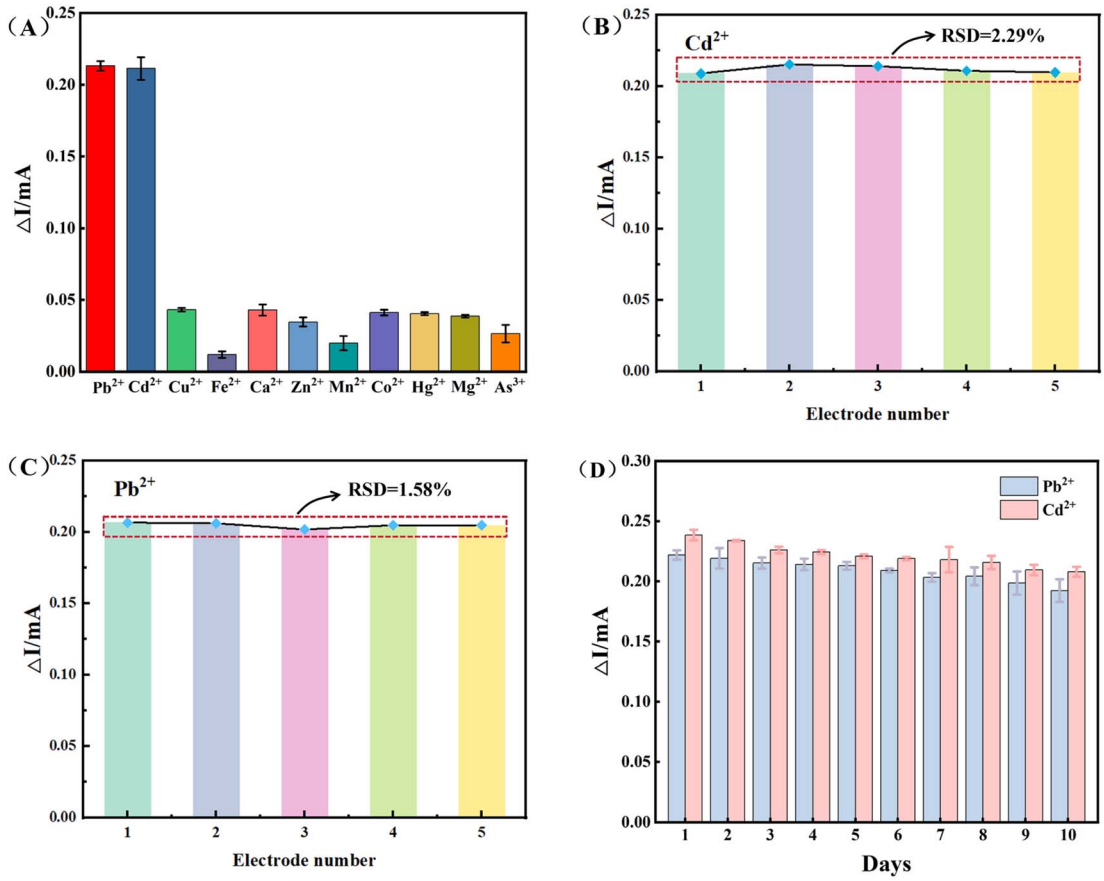

Fig. 5 (A) The selectivity of the aptasensor toward 10 nM Cd^{2+} and 10 nM Pb^{2+}, and the interfering substances Cu^{2+}, Mn^{2+}, Co^{2+}, Fe^{2+}, Ca^{2+}, Zn^{2+}, Hg^{2+}, Mg^{2+}, and As^{3+} (1 μM). (B) Reproducibility by five parallel measurements for the detection of 10 nM Cd^{2+} and (C) 10 nM Pb^{2+} ($n = 3$). (D) Stability for ten days for the detection of 10 nM Cd^{2+} and 10 nM Pb^{2+}.

play a key role in facilitating signal amplification. Thirdly, the use of the labeled probe molecules (NB and Fc) combined with the DPV technique further contributes to the sensitivity improvement.

3.5. Analysis performances of the duplexed-electrochemical aptasensor

In the context of evaluating the performance of a sensor, specificity is a pivotal indicator due to the potential for nonspecific binding to compromise the precision of detection outcomes. To investigate the analytical specificity of the developed duplexed-electrochemical aptasensor for Cd^{2+} and Pb^{2+}, common heavy metal ions such as Cu^{2+}, Mn^{2+}, Co^{2+}, Fe^{2+}, Ca^{2+}, Zn^{2+}, Hg^{2+}, Mg^{2+}, and As^{3+} were selected as references. As demonstrated in Fig. 5A, the aptasensor exhibited no substantial signal change in sensitivity despite the presence of an excess (100-fold) of the other ions. However, significant signal changes were triggered in the presence of the target Cd^{2+} and Pb^{2+}, even at low concentrations. Consequently, the dual-signal aptasensor demonstrated notable specificity for Cd^{2+} and Pb^{2+}.

To evaluate the reproducibility of the sensor, five identical modified electrodes were prepared to fabricate the sensor using the same procedure, and five parallel measurements of its detection performance in 10 nM Cd^{2+} and Pb^{2+} were performed. The results are shown in Fig. 5B and C, with relative standard deviations (RSDs) ($n = 3$) of Cd^{2+} and Pb^{2+} were found to be approximately 2.29% and 1.58%, respectively, thereby indicating the excellent reproducibility of the fabricated sensors. In addition, the stability of the sensors was investigated by subjecting the electrodes to a refrigeration temperature of 4 °C for a period of ten days, and the current response was recorded daily to ascertain the ability of the modified electrodes to maintain the stability of the fabricated sensors. After ten days, the current signals of Cd^{2+} and Pb^{2+} were 87.15% and 86.63% of the original signals, respectively, and the RSD estimates of the two were 1.68% and 2.74%, respectively. These results demonstrated that the stability of the developed aptasensor was acceptable.

3.6. Real sample analysis

To explore the potential of the sensors developed in this work in real-life, scenarios, they were applied to the detection and analysis of Cd^{2+} and Pb^{2+} in real samples. Tap water, river water, and lettuce were selected as the research objects to ensure consideration of the analytical reliability and practical value of the sensors. Consequently, a standard addition method was employed to introduce varying concentrations (100, 1000, and 10 000 pM) of Cd^{2+} and Pb^{2+} into the samples to conduct a comprehensive recovery assessment, and the detailed outcomes are presented in Table S5. The data demonstrated that the recoveries of Cd^{2+} ranged from 91.413% to 104.837%, and those of Pb^{2+} ranged from 95.928% to 106.397%. The RSD were found to be within a reasonable range. To verify the performance of the aptasensor, we conducted consistency test using inductively coupled plasma mass spectrometry (ICP-MS), and the detection results were highly in agreement with those of the ICP-MS, indicating that the dual-signal electrochemical aptasensor exhibited excellent accuracy in resolving Cd^{2+} and Pb^{2+} in water and vegetable samples.

4. Conclusions

In this study, the successful synthesis of LEG@Ti_3C_2 MXene nanocomposites was achieved through the utilisation of a straightforward sonication method. This material possesses a substantial surface area, which can be utilised for the loading of a considerable number of aptamers when employed as a sensing platform. This results in substantial enhancement in detection sensitivity. In view of this property, a dual-signal electrochemical aptasensor with LEG@Ti_3C_2 MXene-modified ITO as a sensing substrate was developed to achieve simultaneous measurement of two metal ions, Cd^{2+} and Pb^{2+}. Specifically, a dual-signal interface was successfully constricted by covalently immobilizing NH_2-functionalised Cd^{2+} and Pb^{2+} complementary chains onto –COOH in LEG@Ti_3C_2 MXene and simultaneously utilizing the specific binding of NB to Cd-Apt, and of Fc to Cd-Apt, as the electrochemical signal sources of the two ions. The aptasensor's highly specific recognition of the target and the significant difference between the electrochemical potentials of NB and Fc result in the sensor's capability to detect Cd^{2+} and Pb^{2+} independently and simultaneously. In the presence of Cd^{2+} and Pb^{2+}, aptamer binding triggers a significant conformational change, inducing the dissociation of Cd-Apt-NB and Pb-Apt-Fc from the electrodes, resulting in a decrease in I_{NB} and I_{Fc}. The sensor exhibits a linear range of 0.01 pM to 10 μM, with detection limits as low as 0.689 pM for Cd^{2+} and 1.548 pM for Pb^{2+}. It demonstrated excellent selectivity and stability. Furthermore, the aptasensor was employed for the analysis of Cd^{2+} and Pb^{2+} in real samples, yielding satisfactory recoveries, thus substantiating its considerable potential in the realm of environmental monitoring of Cd^{2+} and Pb^{2+}.

Author contributions

Fang Li: conceptualization, methodology, supervision, project administration, writing – review & editing, validation. Panpan Dong: data curation, formal analysis, writing – original draft, validation. Zijian Wu: supervision, writing – review & editing, validation. Lu Xue: investigation, data curation, validation. Mingming Luo: investigation, data curation, validation. Yijun Tan: investigation, data curation, validation.

Conflicts of interest

The authors declare no conflicts of interest.

Data availability

The authors confirm that the data supporting the findings of this study are available within the article and the SI. The supplementary information includes XRD patterns, FT-IR spectra, CV curves, table of DNA sequence and table for comparison with previous reports. See DOI: **https://doi.org/10.1039/d5ra04002g**.

Acknowledgements

This research was funded by the Tianjin Municipal Education Commission Scientific Research Program Project [grant number 2024KJ076] and the Tianjin Enterprise Science and Technology Commissioner Project [grant number 24YDTPJC00770].

References

1 N. H. Ramli, J. Y. Loo, N. Mohamad Nor and K. Abdul Razak, *J. Mater. Sci.:Mater. Electron.*, 2024, **35**, 73.
2 D. Singh, S. Shaktawat, S. K. Yadav, R. Verma, K. R. B. Singh and J. Singh, *Int. J. Biol. Macromol.*, 2024, **265**, 130867.
3 C.-Y. Wang, B.-Y. Fang, M.-H. Yao and Y.-D. Zhao, *Sens. Actuators, B*, 2016, **228**, 643–648.
4 J. Yuan, J. Zhang, R. Liang, H. Shen, Z. Suo and H. Jin, *Microchem. J.*, 2025, **209**, 112635.
5 L. M. Costa, F. A. Borges, M. H. da Silva Cavalcanti, A. C. do Lago, C. R. T. Tarley, G. de Fátima Lima Martins and E. C. Figueiredo, *Anal. Chim. Acta*, 2023, **1251**, 340709.
6 M. Yuan, X. Peng, F. Ge, M. Zhao, Q. Li and Z. Wang, *Chin. Chem. Lett.*, 2020, **31**, 2814–2818.
7 H. L. Byers, L. J. McHenry and T. J. Grundl, *Food Chem.:X*, 2019, **1**, 100001.
8 M. Ahmed, Y. H. Chin, X. Guo and X.-M. Zhao, *J. Environ. Sci.*, 2017, **55**, 1–10.
9 D. K. Sarfo, A. Sivanesan, E. L. Izake and G. A. Ayoko, *RSC Adv.*, 2017, **7**, 21567–21575.
10 Z. Chen, Z. Zhang, J. Qi, J. You, J. Ma and L. Chen, *J. Hazard. Mater.*, 2023, **441**, 129889.
11 J. Baranwal, B. Barse, G. Gatto, G. Broncova and A. Kumar, *Chemosensors*, 2022, **10**, 363.
12 M. A. Fathy and P. Bühlmann, *Biosensors*, 2025, **15**, 51.
13 H. Li, P. Zuo, S. Qu, F. Qin, N. Li and W. Shen, *Appl. Surf. Sci.*, 2023, **615**, 156426.
14 L. Ma, W.-Y. Pei, J. Yang and J.-F. Ma, *Food Chem.*, 2024, **441**, 138352.
15 S. M. Taghdisi, N. M. Danesh, P. Lavaee, M. Ramezani and K. Abnous, *Sens. Actuators, B*, 2016, **234**, 462–469.
16 Q. Guo, J. Yin, Y. Zhang, Y. Wang, H. Zhai, L. Yan, M. Tian, Y. Guo, X. Sun and Y. Zhang, *J. Appl. Electrochem.*, 2024, **54**, 1833–1843.
17 S. Sawan, R. Maalouf, A. Errachid and N. Jaffrezic-Renault, *TrAC, Trends Anal. Chem.*, 2020, **131**, 116014.
18 Y. Bi, B. Xing, H. Zeng, B. Xu, J. Jia, Y. Wu, G. Huang, C. Zhang, H. Guo and Y. Cao, *Fuel*, 2024, **378**, 132933.
19 Y. Wang, L. Wang, W. Huang, T. Zhang, X. Hu, J. A. Perman and S. Ma, *J. Mater. Chem. A*, 2017, **5**, 8385–8393.
20 S. Teka, A. Gaied, N. Jaballah, S. Xiaonan and M. Majdoub, *Mater. Res. Bull.*, 2016, **74**, 248–257.
21 L. Wen, J. Dong, H. Yang, J. Zhao, Z. Hu, H. Han, C. Hou, X. Luo and D. Huo, *Sci. Total Environ.*, 2022, **851**, 158325.
22 H. L. Chia, C. C. Mayorga-Martinez, N. Antonatos, Z. Sofer, J. J. Gonzalez-Julian, R. D. Webster and M. Pumera, *Anal. Chem.*, 2020, **92**, 2452–2459.
23 S. Alwarappan, N. Nesakumar, D. Sun, T. Y. Hu and C.-Z. Li, *Biosens. Bioelectron.*, 2022, **205**, 113943.
24 Y. Shi, Y. Ran, Z. Zhang and D.-Z. Du, *Theor. Comput. Sci.*, 2020, **803**, 1–9.
25 S. Zukauskas, A. Rucinskiene, S. Ramanavicius, A. Popov, G. Niaura, I. Baginskiy, V. Zahorodna, S. Dukhnovskiy, O. Gogotsi and A. Ramanavicius, *Sci. Total Environ.*, 2024, **950**, 175190.
26 D. Chen, H. Feng and J. Li, *Chem. Rev.*, 2012, **112**, 6027–6053.
27 J. You, J. Li, Z. Wang, M. Baghayeri and H. Zhang, *Chemosphere*, 2023, **335**, 139133.
28 S. Kesavan, N. S. K. Gowthaman, S. Alwarappan and S. A. John, *Sens. Actuators, B*, 2019, **278**, 46–54.
29 Y. Liang, X. Lin, H. Liao, M. Hasan, S. Gong and X. Zhou, *Chem. Eng. J.*, 2025, **507**, 160606.
30 Y. Pan, L. Wang, S. Chen, Y. Wang and X. Wei, *Microchem. J.*, 2024, **202**, 110705.
31 Z. Liu, F. Zhong, Z. Wu, W. Pang, J. He, M. Deng, S. Huang, J. Cao, Z. Yan, M. Jin and L. Shui, *Sens. Actuators, B*, 2025, **422**, 136558.
32 B. W. N. H. Hemasiri, J.-K. Kim and J.-M. Lee, *Nano-Micro Lett.*, 2017, **10**, 18.
33 D. Akın Kara, K. Kara, G. Oylumluoglu, M. Z. Yigit, M. Can, J. J. Kim, E. K. Burnett, D. L. Gonzalez Arellano, S. Buyukcelebi, F. Ozel, O. Usluer, A. L. Briseno and M. Kus, *ACS Appl. Mater. Interfaces*, 2018, **10**, 30000–30007.
34 J. H. Lee, A. B. M. H. Islam, T. K. Kim, Y.-J. Cha and J. S. Kwak, *Photonics Res.*, 2020, **8**, 1049–1058.
35 R. Salles, W. C. Poh, M. Laurans, F. Volatron, A. Miche, S. Alves, C. Carino, L. Tortech, G. Izzet, P. S. Lee and A. Proust, *Inorg. Chem. Front.*, 2024, **11**, 255–268.
36 Y. Liu, N. Aghdassi, Q. Wang, S. Duhm, Y. Zhou and B. Song, *Org. Electron.*, 2016, **35**, 6–11.
37 F. Li, J. Zhang and S. Hu, *ACS Sens.*, 2021, **6**, 1218–1227.
38 F. Li, P. Dong, Z. Wu, L. Xue, M. Luo, Y. Tan, H. Li and X. Yang, *LWT–Food Sci. Technol.*, 2025, **216**, 117340.
39 F. Gao, F. Zhan, S. Li, P. Antwi-Mensah, L. Niu and Q. Wang, *Biosens. Bioelectron.*, 2022, **209**, 114280.
40 C. R. J Yan, K. Maleski, C. B. Hatter, B. Anasori, P. Urbankowski, A. Sarycheva and Y. Gogotsi, *Adv. Funct. Mater.*, 2017, **27**, 1701264.
41 K. Wang, B. Zheng, M. Mackinder, N. Baule, H. Qiao, H. Jin, T. Schuelke and Q. H. Fan, *Energy Storage Mater.*, 2019, **20**, 299–306.
42 N. A. Karthick, R. Thangappan, M. Arivanandhan, A. Gnanamani and R. Jayavel, *J. Inorg. Organomet. Polym. Mater.*, 2018, **28**, 1021–1028.
43 M. J. Varjovi, R. E. Sabzi and S. M. Borghei, *J. Iran Chem. Soc.*, 2018, **15**, 1765–1774.
44 Y. Cao, Q. Deng, Z. Liu, D. Shen, T. Wang, Q. Huang, S. Du, N. Jiang, C.-T. Lin and J. Yu, *RSC Adv.*, 2017, **7**, 20494–20501.
45 T. Saito, Y. Shimizu, K. Tsukakoshi, K. Abe, J. Lee, K. Ueno, R. Asano, B. V. Jones, T. Yamada, T. Nakano, J. Tong, A. Hishiki, K. Hara, H. Hashimoto, K. Sode, T. Toyo'oka, K. Todoroki and K. Ikebukuro, *Biosens. Bioelectron.*, 2022, **203**, 114027.